

Abstract

We present the electron density (n_e) altitude profiles of Saturn's ionosphere at near equatorial latitudes from all 23 orbits of Cassini's Grand Finale. The data are collected by the Langmuir probe part of the Radio and Plasma Wave Science investigation. A high degree of variability in the electron density profiles is observed. However, organizing them by consecutive altitude ranges revealed clear differences between the southern and northern hemispheres. The n_e profiles are shown to be more variable and connected to the D-ring below 5000 km in the southern hemisphere compared to the northern hemisphere. This observed variability is explained to be a consequence of an electrodynamic interaction with the D ring. Moreover, a density altitude profile is constructed for the northern hemisphere indicating the presence of three different ionospheric layers. Similar properties were observed during Cassini's Final Plunge, where the main ionospheric peak is crossed at ~ 1550 km altitude.

1 Introduction

Prior to the Grand Finale, the final phase of the Cassini mission, no in-situ measurements of the Kronian ionosphere had been made. Properties of Saturn's ionosphere were inferred based on three different remote observation methods: radio occultation [Kliore *et al.*, 1980; Nagy *et al.*, 2006; Kliore *et al.*, 2009, 2014], radio emission from Saturn electrostatic discharges [Kaiser *et al.*, 1984; Fischer *et al.*, 2011] and mm-band observations of protonated molecular hydrogen (H_3^+) [O'Donoghue *et al.*, 2013]. However, only the radio occultation technique has yielded the altitude structure of the electron density. Pioneer 11 [Kliore *et al.*, 1980] and Voyager 1 & 2 [Lindal *et al.*, 1985] provided the first vertical structures of Saturn's ionosphere. During the early phase of the Cassini mission, density profiles were inferred for near dusk, dawn, equatorial, mid and high latitude conditions [Nagy *et al.*, 2006; Kliore *et al.*, 2009]. These observations have shown a decrease in the average electron densities at low latitude ($< 20^\circ$), with lower densities on the dawn side than dusk, and the presence of variable fine structure below about 2500 km altitude (relative to the height of their calculated 1-bar pressure surface of Saturn). The assumption of spherical symmetry (along the line of sight) limits the use of radio occultation measurements in studying features of the ionosphere that may be spatially localized, such as the effect of the D ring on the Kronian ionosphere.

In April 2017, Cassini started its Grand Finale phase executing a series of 23 orbits passing between the planet and its rings, with inclination of 61.7 degrees from the planet's equatorial plane. An illustration of all the proximal perikrones is shown in Figure 1. The distance from the center of Saturn varied from 64 668 km (~ 1.073 Rs) for the closest orbits to the D ring to 62 076 km (~ 1.03 Rs) for the deepest orbits. During the last orbit (Rev 293), known as the Final Plunge, Cassini dove into the planet's atmosphere, sending data for as long as its thrusters could keep the spacecraft's main antenna pointed at Earth. The Radio and Plasma Waves Science/Langmuir Probe (RPWS/LP) instrument onboard the spacecraft provided unprecedented in-situ observations of Saturn's ionosphere. Wahlund *et al.* [2017] presented the first detection of the top-side Kronian ionosphere based on data from the first 11 perikrones [271-282]. They showed a clear variability in the electron number density profiles and evidence for a D ring interaction at the equatorial plane. Moreover, a north/south asymmetry was shown to be a consequence of the A and B rings shadows that reduce the ionization in the southern part of the Kronian atmosphere. In this paper we present the first electron density altitude profile from all proximal orbits. We compare the northern and the southern hemispheres and discuss how the D ring affects/controls the altitude structure of Saturn's ionosphere.

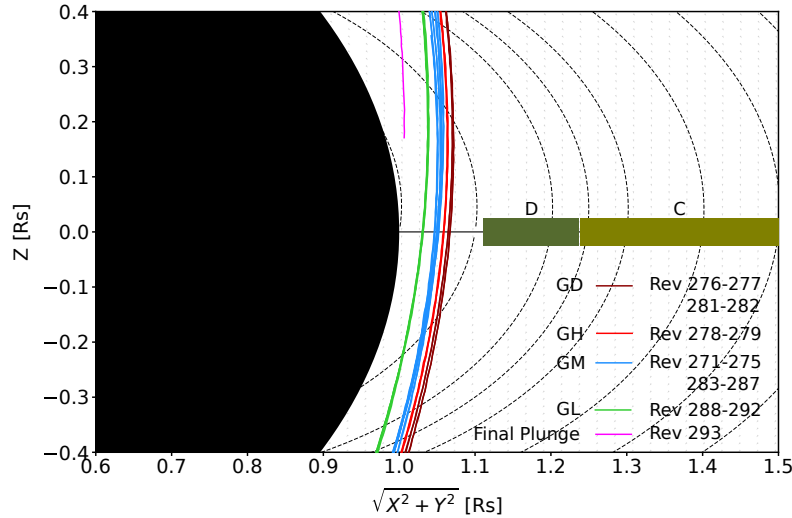


Figure 1. Illustration of the 23 perikrones during the Grand Finale of Cassini passing between Saturn (in black) and the D ring (dark green). The coordinates are defined as X in the solar equatorial plane positive towards the Sun, Z northward along the spin axis of the planet and Y completing the right-handed orthogonal set. GD, GH, GM and GL represent four groups: the closest orbits to the D ring (GD), the high (GH), mid (GM) and low (GL) altitude groups. The magnetic field lines are computed using the internal magnetic field model of *Burton et al.* [2010].

2 RPWS experiment methods

The RPWS investigation provides at least three independent methods to estimate the electron density: two derived from the LP and one estimated from features in the plasma wave spectrum - either a cutoff at the plasma frequency or the upper hybrid frequency band (see *Persoon et al.* [2018]).

2.1 Langmuir Probe sensor

The first method makes use of the LP sensor which provides *in situ* information on the ambient plasma parameters. The probe is a TiN-coated Ti sphere with diameter of 5 cm mounted on a 1.5 m boom [*Gurnett et al.*, 2004; *Wahlund et al.*, 2009; *Morooka et al.*, 2011]. It measures the current of the charged particles in two different modes, the voltage sweep mode and the high resolution 20 Hz continuous mode. In the sweep mode, the LP samples the total current from the plasma (incoming and outgoing) as a function of an applied bias voltage, U_{bias} (± 32 V or ± 4 V). When applying a positive (or negative) bias potential, the probe will attract electrons and repel ions (or repel electrons and attract ions) from the ambient plasma, and so the resulting current is measured. From the voltage - current characteristics of the LP a number of plasma parameters can be estimated and derived (the spacecraft potential U_{sc} , the electron number density n_e , the electron temperature T_e , the ion density n_i , the ion ram speed v_i , and the average ion mass m_i). More details regarding the derivation of the parameters can be found in [*Holmberg et al.*, 2012; *Shebanits et al.*, 2013, 2016]. In the continuous mode, the electron current (I_e) is sampled at a constant bias voltage (+11 V for ± 32 V sweep mode, +4 V for ± 4 V sweep mode) with 20 samples per second and is proportional to:

$$I_e \propto \sqrt{T_e} n_e \left[1 + \frac{1}{T_e} (U_{sc} + U_{bias}) \right] \quad (1)$$

Using T_e and U_{sc} estimates from the voltage sweeps (with lower temporal resolution) and assuming T_e and $U_{sc} \approx$ constant between the sweeps, we can derive n_e with a resolution of 20 Hz [Ågren *et al.*, 2007; Ågren *et al.*, 2009].

2.2 Characteristic frequencies of plasma waves

Another method to estimate n_e is based on observations in the electric field spectra of the sharp upper frequency cut-off of whistler mode or a line at the upper hybrid frequency (f_{uh}). For the former, the upper cut-off frequency corresponds to the local $\min(f_{pe}, f_{ce})$, where f_{pe} and f_{ce} represent respectively the electron plasma and cyclotron frequencies. When the magnetic field is strong, $f_{pe} < f_{ce}$, so n_e is calculated from the cutoff at f_{pe} by using the relation $n_e [\text{cm}^{-3}] = (f_{pe} [\text{Hz}]/8980)^2$. When $f_{pe} \geq f_{ce}$, then a band at f_{uh} is apparent. Hence f_{uh} can be used as it is related to f_{pe} by $f_{uh}^2 = f_{pe}^2 + f_{ce}^2$ and f_{ce} is well known from the magnetometer measurements of $|B|$ since $f_{ce} [\text{Hz}] = 28|B| [\text{nT}]$ [Persoon *et al.*, 2005; Gurnett *et al.*, 2005; Persoon *et al.*, 2018].

3 Observations

3.1 Electron density variability

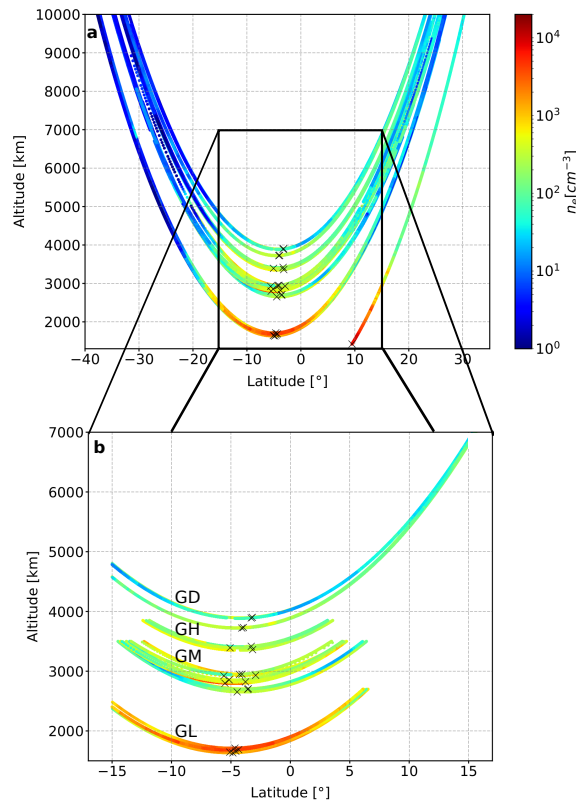


Figure 2. (a) Electron density (color coded) as a function of altitude (h) and latitude (ϕ). (b) Consecutive altitude portions of the density profiles for the latitude range $-15^\circ \leq \phi \leq 15^\circ$ and altitude range $1200 \text{ km} \leq h \leq 7000 \text{ km}$. The periapsis on each orbit is marked by a black cross and GD-GL represent the different altitude groups defined in Figure 1.

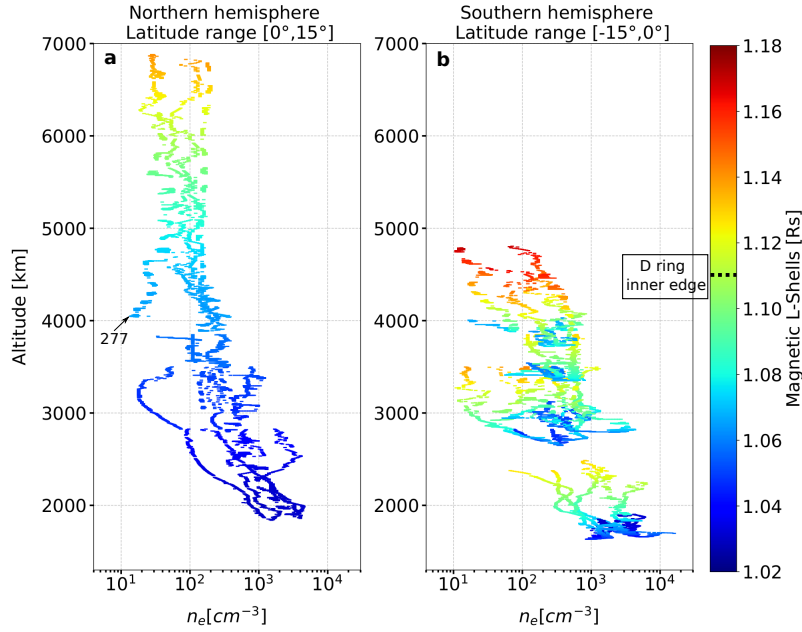
In this work, the electron densities are estimated from the LP high resolution 20 Hz sampling mode for all the 23 perikrones. At times when LP was partly (Revs 273, 284,

286, 289) or entirely (Revs 272, 285) in the wake of the spacecraft, we use the electron densities derived from the upper cut-off frequency of the whistler waves or the f_{uh} line [Persoon *et al.*, 2018] which give identical results, although at lower time resolution [Wahlund *et al.*, 2017]. The n_e profiles of the 23 passes are presented in Figure 2-a as a function of altitude (h) and geographic latitude (ϕ). The altitudes are computed by considering Saturn as an oblate spheroid with an equatorial radius of 60 268 km and a polar radius of 54364 km. By convention, the reference altitude is set to a distance of 60 268 km from the center of Saturn in the equatorial plane which is considered as the 1-bar pressure level. The north-south asymmetry and the large variability in n_e between the orbits (and within single orbit), reported by Wahlund *et al.* [2017] on the first few perikrones can be seen in Figure 2-a. For each orbit the maximum density occurs around the closest approach (ca , black crosses) in the southern hemisphere between $\sim -4^\circ$ and -5° with a local time centered around local noon, and a solar zenith angle varying between 30° and 35° . The electron number density varies from $\sim 60 \text{ cm}^{-3}$ at the highest altitudes ($h > 3900 \text{ km}$) up to $2 \times 10^4 \text{ cm}^{-3}$ for the lowest altitudes ($h < 2000 \text{ km}$). To exclude the effect from the B ring shadow [Hadid *et al.*, 2018], we limit our analysis to near equatorial latitudes $-15^\circ \leq \phi \leq 15^\circ$ (Figure 2-b). Moreover, in order to study the electron density altitude profile of Saturn's topside ionosphere, we separate, classify and label the proximal orbits, excluding the Final Plunge (Rev 293), into four different groups based on the ca altitude: GD, the closest orbits to the D ring, GH, the high altitude, GM, the mid altitude, and GL, the low altitude ones (Figure 1). Since the Final Plunge covers continuously all the altitude ranges, we consider it as a reference and include it in the analysis in section 3.3 where we compare its profile with the average one.

3.2 D-ring effect on the ionospheric electron density structure

To investigate if the rings play a role in structuring the Kronian topside ionosphere, we show in Figure 3 the northern and southern hemisphere h , n_e profiles (excluding for now the Final Plunge) as a function of the magnetic L -Shells (L). In order to get a continuous altitude profile and to confine the study in specific altitude/latitude range, we select, for each group, consecutive altitude ranges as shown in Figure 2-b: $1600 \text{ km} \leq h \leq 2830 \text{ km}$ for the deepest altitude group (GL); $2700 \text{ km} \leq h \leq 3500 \text{ km}$ for the mid altitude group (GM), $3350 \text{ km} \leq h \leq 3850 \text{ km}$ for the high altitude cases (GH), and $3750 \text{ km} \leq h \leq 7000 \text{ km}$ for the closest orbits to the D-ring (GD).

The density increases with decreasing altitude over about 2 orders of magnitude both in the northern and southern hemisphere. However, despite this similarity, clear differences between the two hemispheres can be observed. Contrary to the southern hemisphere (Figure 3-b), the altitude profiles in the northern one (Figure 3-a) are stable and organized. For $4000 < h < 7000 \text{ km}$ the individual density profiles display only small variations and overlap near 4000 km. Rev 277 is an exception, since it is one of the crossings closest to the D ring. It has been shown by Wahlund *et al.* [2017] to be characterized by clear signatures of negative heavy ions/dust grains ($> 18 \text{ amu}$) near the equatorial plane, probably originating from the D ring. This was evidenced by the differences in ion and electron densities measured by the Langmuir probe. Below around 4000 km the n_e profiles start to be highly variable down to 2000 km, below which they re-organize and become smoother. Furthermore, in the northern hemisphere (Figure 3-a) below $\sim 5000 \text{ km}$, the n_e profiles are related to a narrower and lower range of L -Shell values ($1.03 \text{ Rs} \lesssim L \lesssim 1.08 \text{ Rs}$) compared to the southern hemisphere (Figure 3-b), where for each altitude group they vary from $\sim 1.03 \text{ Rs}$ up to $\sim 1.18 \text{ Rs}$. The spreading and variability in the electron density profiles are mostly observed in the southern hemisphere at all the altitude ranges whereas they are localized between around [2200-4000 km] in the northern hemisphere. Noting that the inner edge of the D ring is around 66 900 km (1.11 Rs), implies that up to 5000 km, the northern density profiles are not connected to magnetic L -Shells that cross the D-ring while they do in the southern hemisphere.



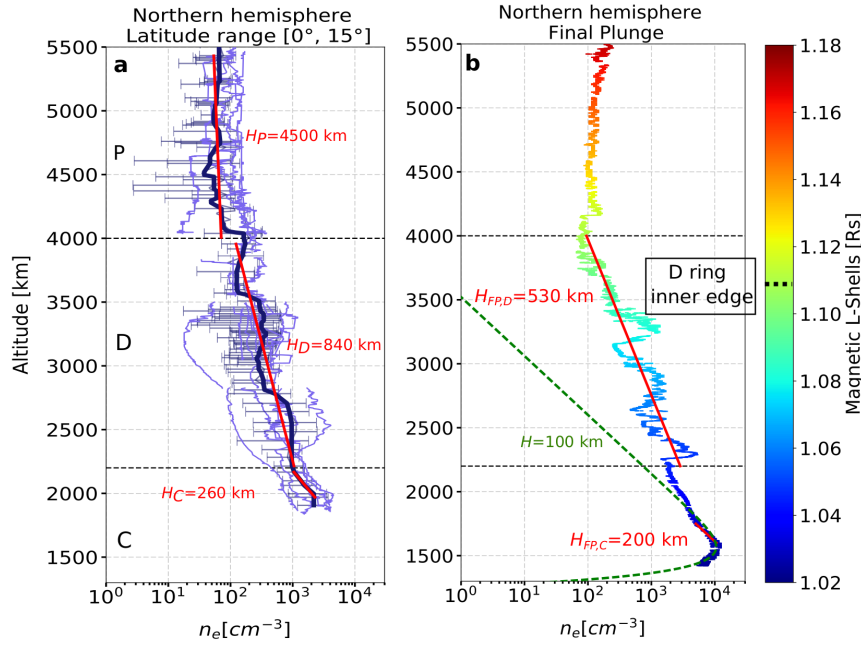
147 **Figure 3.** Altitude density profiles of all the proximal orbits (22, all but the Final Plunge) at equatorial
 148 latitudes for the (a) northern and (b) southern hemispheres. The color code signifies the computed magnetic
 149 L-Shells using the internal magnetic field model of *Burton et al.* [2010].

170 3.3 Ionospheric density altitude profile model

171 Since the h , n_e variations at equatorial latitudes in the northern hemisphere are
 172 not connected to L-Shells that cross the D ring (at least not up to 5500 km), we assume
 173 that they represent “standard” (or typical) profiles of the Kronian top side ionosphere.
 174 We show in Figure 4-a the averaged h , n_e top side ionospheric profile and model up to
 175 5500 km. As one can see, it exhibits a layered structure with distinct regions denoted by
 176 **P** ($h > 4000$ km), **D** ($2200 \text{ km} \lesssim h \lesssim 4000$ km) and **C** ($h < 2200$ km). The notations **P**, **D**
 177 and **C** refer respectively to “Plasmasphere”, “Diffusive” and “Chemical” discussed in sec-
 178 tion 4. Region **P** is characterized by near-constant n_e values with respect to altitude before
 179 it starts to increase around 4500 km, region **D** is highly variable and structured, whereas
 180 region **C** is more stable and regular. Ignoring physical processes (e.g. wave phenomena,
 181 turbulence), and the variation of gravity and temperature with altitude and assuming dif-
 182 fusive equilibrium, charge neutrality ($n_i = n_e$), thermal equilibrium ($T_i \sim T_e$) and 1D ge-
 183 ometry, we estimate the plasma scale height by fitting with an exponential curve for each
 184 of the regions **P**, **D** and **C**. We recognize that these are density plots versus altitude and
 185 assuming diffusive equilibrium as a function of altitude is questionable but it is useful to
 186 obtain such scale height values. We use the following expression:

$$194 \quad n = n_0 e^{(-h-h_0)/H_{P,D,C}} \quad (2)$$

195 Here H is the plasma scale height, the subscript 0 denotes the reference altitude and P,
 196 D and C corresponds to the different ionospheric regions. Setting the reference altitude
 197 to the 1-bar “surface” of Saturn ($h_0 = 0$ km), we find from the following values: H_P
 198 ~ 4500 km (consistent with the scale height estimation of the ionosphere in the northern
 199 hemisphere by *Persoon et al.* [2018]), $H_D \sim 840$ km, $H_C \sim 260$ km, and $n_{0P} \sim 825 \text{ cm}^{-3}$,
 200 $n_{0D} \sim 1.4 \times 10^4 \text{ cm}^{-3}$, $n_{0C} \sim 3.8 \times 10^6 \text{ cm}^{-3}$. The derived plasma scale heights can be
 201 compared with a theoretical estimate:



187 **Figure 4.** (a) The averaged h, n_e profile (dark blue curve) over all the proximal orbits (purple curves) in
 188 the northern hemisphere (except for 293). The error bars represent the standard deviations of the averaged
 189 model. (b) The h, n_e profile of the Final Plunge orbit. The color code shows the corresponding magnetic
 190 L-Shell values. The Chapman model is represented by the green dashed curve. **P**, **D**, and **C** denote different
 191 ionospheric regions delimited by the black dashed lines and the red lines are exponential fitting curves in the
 192 different layers. $H_{P,D,C}$ and $H_{FP,D,C}$ represent the estimated scaled heights in the different layers for the
 193 northern hemisphere and the “Final Plunge” respectively.

$$202 \quad H_{theo} = \frac{2kT_p}{m_i g} \quad (3)$$

203 Where k is the Boltzmann’s constant, T_p is the plasma temperature, m_i is the mean ion
 204 mass and g is the gravitational acceleration at Saturn. Assuming the dominance of H^+ and
 205 $T_i \approx T_e \approx 1160$ K [Wahlund *et al.*, 2017], we obtain $H_{theo} \approx 1917$ km. This is significantly
 206 larger than the values of 840 km and 260 km derived in regions **D** and **C**, respectively,
 207 possibly related to the thermal equilibrium assumption we have made ($T_i \approx T_e$) and/or
 208 hinting towards a significant component of molecular ions and a mean positive ion mass,
 209 in region **D** closer to 2-3 amu (mainly H^+ and H_3^+) and in region **C** $\gtrsim 5-10$ amu [Morooka
 210 *et al.*, 2018a; Waite *et al.*, 2018].

211 In Figure 4-b, we present the “Final Plunge” (FP) orbit which covers almost the
 212 same altitude range from at least 5500 km down to 1300 km. One can clearly relate the
 213 three different ionospheric regions highlighted in the averaged profile (Figure 4-a). Re-
 214 gion **P** where the density looks almost constant with respect to the altitude but increases
 215 above ~ 5500 km [Persoon *et al.*, 2018], **D** where the profile is characterized by the pres-
 216 ence of clear irregular and periodic structures and **C**, where n_e increases exponentially
 217 deeper in the ionosphere with a clear ionospheric peak around 1550 km. The color code
 218 corresponds to the magnetic L-Shell values and shows that region **D** maps well inside
 219 the inner edge of the D ring. The irregular density profiles in the northern hemisphere
 220 are therefore not connected to features in the rings. The scale heights are also estimated
 221 for this orbit by fitting exponential curves (red lines) using the same formula as before

(Eq. 2). For the “Final Plunge”, the obtained values are $H_{FP,D} \sim 530$ km for region **D** and $H_{FP,C} \sim 200$ km for region **C** just above the main peak. We note that very similar scale height to $H_{FP,D}$ was estimated by *Nagy et al.* [2006] to 500 km, for the dusk occultation and more recently by *Persoon et al.* [2018] to about 540 km, using the characteristic frequencies of the plasma waves. Finally we fit the observed ionospheric peak, below 2000 km, with the Chapman model shown by the green curve. The best fit was obtained using the solar zenith angle of the Final Plunge at those altitudes which is around 24° , $H = 100$ km, and setting the reference altitude at the ionospheric peak $h_0 = 1550$ km and the peak density value $n_0 = 1.5 \times 10^4 \text{ cm}^{-3}$. At photochemical equilibrium and with $n_e \approx n_i \approx n_0$, $n_0 \approx \sqrt{q/\alpha}$ where q is the production rate and α is the effective ion-electron recombination coefficient. Crudely assuming that the peak ionization rate in Saturn’s sunlit ionosphere is similar as in Titan’s ionosphere ($\sim 30 \text{ cm}^{-3}\text{s}^{-1}$ for similar SZA, see e.g., *Vigren et al.* [2013]) the relation then gives $\alpha \approx 1.3 \times 10^{-7} \text{ cm}^3\text{s}^{-1}$ near the peak. This may be viewed as a crude upper limit of α ; if electrons are lost partly to charging of macromolecules/grains the estimated α can to first approximation be corrected by a multiplicative factor n_e/n_i [*Vigren et al.*, 2014].

4 Discussion and conclusions

Despite the large variability of the electron number densities observed from one orbit to another at equatorial latitudes, the overall altitude profiles showed an increase of n_e towards lower altitude, with a maximum density $> 10^3 \text{ cm}^{-3}$ occurring below 2000 km (Figure 2) similar to previous radio occultation measurements of the Kronian ionosphere [*Lindal et al.*, 1985; *Nagy et al.*, 2006; *Kliore et al.*, 1980, 2009]. However, looking more closely at the northern and the southern hemispheres, the RPWS/LP and the frequency characteristics of the plasma waves when used, have revealed a clear north/south asymmetry regarding the structure of the density profiles (Figure 3). The southern hemisphere (Figure 3-b) is observed to be much more variable than the northern one regardless of the magnetic L-Shell values and is shown to be connected to magnetic L-Shells that cross the D ring ($L \geq 1.11$ Rs). Moreover, since at those L values, the ionosphere is mainly dominated by H^+ [*Wahlund et al.*, 2017], it implies the dominance of electrodynamic processes via flux-tubes which traverse the electrically conductive D ring over chemical processes [*Waite et al.*, 2018]. In fact, using the RPWS radio measurements, *Sulaiman et al.* [2018b] show the presence of clear signatures of whistler waves (classified as auroral hiss and VLF saucers) in the southern hemisphere at similar altitudes, directly linked to the planet on field lines connected to the D ring, hence suggesting as well an electrodynamic coupling with the ring. This highlights the effect of the D ring interaction on structuring and increasing the variability of the electron density profiles in the topside southern hemisphere. Furthermore, it confirms the role of Saturn’s strong magnetic field in facilitating the coupling between the rings and the Kronian ionosphere. It is worth noting that this asymmetry is actually a direct consequence of the northward offset of Saturn’s magnetic equator by about 2700 km (0.036 Rs) [*Burton et al.*, 2010].

Thanks to the very high time resolution of the LP 20 Hz mode, the topside ionospheric density profile model constructed in the northern hemisphere (Figure 4-a) and the Final Plunge event (Figure 4-b) highlight the presence of three different layers, regular (**P** and **C**) and irregular (**D**) ones, characterized by different plasma processes. Layer **P**, above 4500 km can be interpreted as the inner part of the “plasmosphere” dominated by H^+ with very few collisions and characterized by convection transfer.

Layer **D**, between ~ 4000 km and ~ 2200 km, represents a diffusive equilibrium region, where the electron density decreases exponentially with altitude. We note that since Cassini is crossing field lines rapidly, the estimated scale heights in this layer (840 km and 530 km, Figure 4-a-b respectively) are not equivalent to vertical plasma scale heights. Instead Cassini is sampling the variation in ionospheric densities and temperatures as it traverses the different flux tubes. This could explain the different variations observed in the density profiles consistent with previous radio occultation measurements at similar alti-

275 tude range [Lindal *et al.*, 1985; Nagy *et al.*, 2006; Kliore *et al.*, 2009]. Moreover, it is note-
 276 worthy that unlike the southern ionosphere, for this particular altitude range, the observed
 277 irregularities present sharp gradients in the electron number density. Furthermore since
 278 the variations are connected to magnetic L-Shell values $< 1.07 R_s$, implies that they are
 279 not associated with field lines that connect to the D ring (as one can see in Figure 3-a).
 280 Other than diffusive processes, other physical processes (e.g. turbulence, wave phenomena,
 281 plasma instabilities -Rayleigh Taylor or the Perkins instabilities-, undamped gravity waves,
 282 wind induced drifts along the magnetic field lines) could also induce such irregularities.
 283 *Matcheva et al.* [2001] showed at Jupiter, although at much lower altitudes between about
 284 600 and 900 km, that gravity waves are likely to be important in creating steep, multiple
 285 density peaks. Moreover, *Sulaiman et al.* [2018a] evidence the presence of intense har-
 286 monic emissions covering similar altitude range.

287 Layer C, the region below 2200 km, represents a chemical equilibrium region, domi-
 288 nated by chemical processes. *Morooka et al.* [2018a] observe the dominance of negatively
 289 and positively charged heavy cluster ions in this altitude range and *Cravens et al.* [2018]
 290 interpret it as a non-diffusive layer of heavy molecular ions. Moreover, recently the Ion-
 291 Neutral Mass Spectrometer (INMS) observations implied the presence of organic ions
 292 at those low altitudes [Waite *et al.*, 2018], and the densities of positive dust grains mea-
 293 sured by the Charge Energy Mass Spectrometer (CHEMS), designed to measure only the
 294 positive dust, are shown to be directly proportional to the heavy positive ion population
 295 [Mitchell *et al.*, 2018] below 1700 km. The estimated scale heights in this C layer (260 km
 296 and 200 km, Figure 4-a-b respectively) probably represent the true neutral scale heights.
 297 Noting that the profiles in layer D are dominated by H^+ , and because of the gravity, the
 298 density, the mass and temperature gradients [Morooka *et al.*, 2018b], an ambipolar electric
 299 field will generate in the plasma within regions D and C. As a consequence, this would
 300 result in the h , n_e variability at this boundary region. This transition from chemical to dif-
 301 fusion dominance, is similar to the sub F_2 region in the terrestrial ionosphere [Schunk and
 302 Nagy, 2009].

303 Last but not least, during the Final Plunge orbit (Figure 4-b), the RPWS/LP 20 sam-
 304 ples/s have revealed a density peak of $\sim 1.5 \times 10^4 \text{ cm}^{-3}$ around 1550 km, which we in-
 305 terpret as the “main peak” of the Kronian ionosphere. Our observations represent the
 306 first detailed in-situ measurements of the ionospheric peak of Saturn with high accuracy.
 307 They are consistent with previous ionospheric models where the main peak was observed
 308 around 1900 km and a maximum electron densities around 10^4 cm^{-3} [Moore *et al.*, 2006].
 309 This is further confirmed by ionospheric photochemical equilibrium models compared to
 310 data [Wahlund *et al.*, 2018; Moore *et al.*, 2018].

311 Acknowledgments

312 The RPWS/LP instrument on board Cassini is supported by the Swedish National Space
 313 Board (SNSB). LZH acknowledges funding by the Swedish Research Council (Veten-
 314 skapsrådet, VR) under the contract number 2016-05364. MWM acknowledges funding
 315 by the SNSB under contract Dnr 174/15. OS acknowledges funding by the Royal Soci-
 316 ety. NJTE acknowledges funding by the SNSB under contract Dnr 135/13 and VR under
 317 contract 621-2013-4191. The research at the University of Iowa was supported by NASA
 318 through Contract 1415150 with the Jet Propulsion Laboratory. The research at the Univer-
 319 sity of Michigan was supported by NASA through contract 1416972 with the Jet Propul-
 320 sion Laboratory. Cassini RPWS data will be available on NASA Planetary Data System
 321 <https://pds.jpl.nasa.gov>

322 References

323 Ågren K., Wahlund J.-E., Modolo, R., Lummerzheim, D., Galand, M., Müller-Wodarg,
 324 I., Canu, P., Kurth, W. S., Cravens, T. E., Yelle, R. V., J. H. Waite Jr., Coates, A. J.,
 325 Lewis, G. R., Young, D. T., Bertucci, C., Dougherty, M. K., (2007). On magnetospheric

- 326 electron impact ionisation and dynamics in Titan's ram-side and polar ionosphere - a
327 Cassini case study. *Annales Geophysicae*, 25, 2359–2369. [https://doi.org/10.5194/angeo-](https://doi.org/10.5194/angeo-25-2359-2007)
328 25-2359-2007.
- 329 Ågren K., Wahlund J.-E., Garnier P., Modolo R., Cui J., Galand M., Muller-Wodarg I.,
330 (2009). On the ionospheric structure of Titan. *Planetary and Space Science*, 57, 1821 -
331 1827. <https://doi.org/10.1016/j.pss.2009.04.012>.
- 332 Burton, M. E., Dougherty, M. K., Russell, C. T., (2010). Saturn's in-
333 ternal planetary magnetic field. *Geophysical Research Letters*, 24, 37.
334 <https://doi.org/10.1016/j.pss.2009.04.008>.
- 335 Cravens, T.E., Moore, L., Waite, J.H. Jr., Perryman, R., Perry, M., Wahlund, J.-E., Persoon
336 A., and Kurth, W. S. (2018), The ion composition of Saturn's equatorial Ionosphere as
337 observed by Cassini, *Geophys. Res. Lett.*, this issue.
- 338 Fischer, G., Gurnett, D. A., Zarka, P., Moore, L., Dyudina, U. A., 2011, Peak electron
339 densities in Saturn's ionosphere derived from the low-frequency cutoff of Saturn light-
340 ning *J. Geophys. Res.*, 116, A04315. <https://doi.org/10.1029/2010JA016187>.
- 341 Gurnett, D. A., Kurth, W. S., Kirchner, D. L., Hospodarsky, G. B., Averkamp, T. F.,
342 Zarka, P., Lecacheux, A., Manning, R., Roux, A., Canu, P., Cornilleau-Wehrin, N., Ga-
343 lopeau, P., Meyer, A., Boström, R., Gustafsson, G., Wahlund, J.-E., Åhlen, L., Rucker,
344 H. O., Ladreiter, H. P., Macher, W., Woolliscroft, L. J. C., Alleyne, H., Kaiser, M. L.,
345 Desch, M. D., Farrell, W. M., Harvey, C. C., Louarn, P., Kellogg, P. J., Goetz, K. and
346 Pedersen, A., (2004). The Cassini Radio and Plasma Wave Investigation. *Space Science*
347 *Reviews*, 114, 395-463. <https://doi.org/10.1007/s11214-004-1434-0>.
- 348 Gurnett, D. A., Kurth, W. S., Hospodarsky, G. B., Persoon, A. M., Averkamp, T. F., Cec-
349 conni, B., Lecacheux, A., Zarka, P., Canu, P., Cornilleau-Wehrin, N., Galopeau, P. and
350 Roux, A., Harvey, C., Louarn, P., Bostrom, R., Gustafsson, G., Wahlund, J.-E., M. D.,
351 Farrell, W. M., Kaiser, M. L., Goetz, K., Kellogg, P. J., Fischer, G., Ladreiter, H.-P.,
352 Rucker, H., Alleyne, H., and Pedersen, A., (2005). Radio and Plasma Wave Observa-
353 tions at Saturn from Cassini's Approach and First Orbit. *Science*, 5713, 307, 1255–
354 1259. <https://doi.org/10.1126/science.1105356>.
- 355 Hadid, L. Z., Morooka, M. W., Wahlund, J.-E., Moore, L., Cravens, T. E., Hedman, M.
356 fM., Edberg, N. J. T, Vigren, E., Kurth, W. S., Farrell, W. M., and Eriksson, A. I.,
357 (2018). A and B ring shadowing effects on Saturn's ionosphere: Implications for ring
358 opacity and plasma transport processes. *Geophysical Research Letters*, this issue.
- 359 Holmberg, M.K.G., Wahlund, J.-E., Morooka, M.W., and Persoon, A.M. (2012). Ion den-
360 sities and velocities in the inner plasma torus of Saturn. *Planetary and Space Science*, 73,
361 1. <https://doi.org/10.1016/j.pss.2012.09.016>.
- 362 Kaiser, M. L., Desch, M. D. and Connerney, J. E. P., (1984). Saturn's ionosphere: Inferred
363 electron densities. *Journal of Geophysical Research: Space Physics*, A4,89, 2371–2376.
364 <https://doi.org/10.1029/JA089iA04p02371>.
- 365 Kliore, A. J., Lindal, G. F., Patel, I. R., Sweetnam, D. N., Hotz, H. B., Mcdonough,
366 T. R., (1980). Vertical Structure of the Ionosphere and Upper Neutral Atmosphere
367 of Saturn from the Pioneer Radio Occultation. *Science*, 4429, 207, 446–449.
368 <https://doi.org/10.1126/science.207.4429.446>.
- 369 Kliore, A. J., Nagy, A. F., Marouf, E. A., Anabtawi, A., Barbinis, E., Fleischman, D. U.
370 and Kahan, D. S., (2009). Midlatitude and high-latitude electron density profiles in
371 the ionosphere of Saturn obtained by Cassini radio occultation observations. *Journal of*
372 *Geophysical Research: Space Physics*, A4, 114. <https://doi.org/10.1029/2008JA013900>.
- 373 Kliore, A. J., A. Nagy, S. Asmar, A. Anabtawi, E. Barbinis, D. Fleischman, D. Kahan, and
374 J. Klose (2014), The ionosphere of Saturn as observed by the Cassini Radio Science
375 System, *Geophys. Res. Lett.*, 41, 5778-5782. <https://doi.org/10.1002/2014GL060512>.
- 376 Lindal, G. F., Sweetnam, D. N. and Eshleman, V. R., (1985). The atmosphere of Saturn -
377 an analysis of the Voyager radio occultation measurements. *The Astronomical Journal*,
378 90, 1136-1146. <https://doi.org/10.1086/113820>.

- 379 Matcheva K. I., Strobel, D. F., and Flasar F.M., (2001). Interaction of Gravity Waves with
380 Ionospheric Plasma: Implications for Jupiter's Ionosphere. *Icarus*, 2, 152, 347-365.
381 <https://doi.org/10.1006/icar.2001.6631>.
- 382 Mitchell, D.G., Perry, M., Waite, J. H., Jr. and Perryman, R., Hamilton, D., Westlake, J.,
383 Kollmann, P., Smith, T., Carbary, J. F., Hsu, S., Wahlund, J.-E., Morooka, M. W., Ha-
384 did, L. Z., Persoon, A. M. and Kurth, W. (2018). Cassini/MIMI Dust Measurements in
385 Saturn's Ionosphere and Upper Atmosphere. *Science*, submitted.
- 386 Moore, L., Nagy, A. F., Kliore, A. J., MÅijller-Wodarg, I., 1, Richardson J. D. and
387 Mendillo M. (2006). Cassini radio occultations of Saturn's ionosphere: Model com-
388 parisons using a constant water flux. *Geophysical Research Letters*, V. 33, L22202,
389 <https://doi.org/10.1029/2006GL027375>.
- 390 Moore, L., T. E. Cravens, I. Müller-Wodarg, M. Perry, J. H. Waite, R. Perryman, A. Nagy,
391 D. Mitchell, A. Persoon, and J.-E. Wahlund (2018), Models of Saturn's equatorial iono-
392 sphere based on in situ data from Cassini grand finale. *Geophys. Res. Lett.*
- 393 Morooka, M. W., Wahlund, J.-E., Eriksson, A. I., Farrell, W. M., Gurnett, D. A., Kurth,
394 W. S., Persoon, A. M., Shafiq, M., André, M., Holmberg, M. K. G., (2011). Dusty
395 plasma in the vicinity of Enceladus. *Journal of Geophysical Research: Space Physics*,
396 A12, 116, 347-365. <https://doi.org/10.1029/2011JA017038>.
- 397 Morooka, M. W., Wahlund, J.-E., Hadid, L. Z., Edberg, N. J. T., Vigren E., Andrews, D.
398 J., Persoon, A. M., Kurth, W. S., Gurnett, D. A., Farrell, W. M. Waite, J. H., Perry-
399 man, R. S., Perry, M., Mitchell, D. G. and Hsu, S. (2018). Saturn's Dusty Ionosphere
400 of Heavy Ions. *Geophysical Research Letters*, this issue.
- 401 Morooka, M. W., Wahlund, J.-E., Hadid, L. Z., Edberg, N. J. T., Vigren E., Andrews, D.
402 J., Persoon, A. M., Kurth, W. S., Gurnett, D. A., Farrell, W. M. (2018). The electron
403 temperature of Saturn's ionosphere near the equator. *Geophysical Research Letters*,
404 this issue.
- 405 Nagy, A. F., Kliore, A. J., Marouf, E., French, R., Flasar, M., Rappaport, N. J., An-
406 abtawi, A., Asmar, S. W., Johnston, D., Barbini, E., Goltz, G. and Fleischman, D.,
407 (2006). First results from the ionospheric radio occultations of Saturn by the Cassini
408 spacecraft. *Journal of Geophysical Research: Space Physics*, A6, 111, 1136-1146.
409 <https://doi.org/10.1029/2005JA011519>.
- 410 O'Donoghue, J., Stallard, T. S., Melin, H., Jones, G. H., Cowley, S. W. H., Miller, S.,
411 Baines, K. H. and Blake, J. S. D., (2013). The domination of Saturn's low-latitude iono-
412 sphere by ring 'rain'. *Nature Physics*, A6, 496. 193. <https://doi.org/10.1038/nature12049>.
- 413 Persoon, A.M., D.A. Gurnett, W.S. Kurth, G.B. Hospodarsky, J.B. Groene, P. Canu and
414 M.K. Dougherty (2005), Equatorial electron density measurements in Saturn's inner
415 magnetosphere, *Geophys. Res. Lett.*, 32. <https://doi.org/10.1029/2005GL024294>.
- 416 Persoon, A. M., Kurth, W.S., Gurnett, D.A., Groene, J.B., Sulaiman, A., Wahlund, J.-E.,
417 Morooka, M.W., Hadid, L.Z., A.F. Nagy, A.F., Waite, J.H. Jr, Cravens T.E. (2018).
418 Electron Density Distributions in Saturn's Ionosphere. *Geophysical Research Letters*,
419 this issue.
- 420 Schunk, R.W. and Nagy, A.F., (2009). Ionospheres: Physics, Plasma Physics, and Chem-
421 istry, 2nd Edition. *Cambridge Atmospheric and Space Science Series*, Cambridge Univer-
422 sity Press, isbn: 9781108462105.
- 423 Shebanits, O., Wahlund, J.-E., Mandt, K., Ågren, K., Edberg, N.J.T., Waite, J.H., (2013).
424 Negative ion densities in the ionosphere of Titan-Cassini RPWS/LP results. *Planetary
425 and Space Science*, 84. <https://doi.org/10.1016/j.pss.2013.05.021>.
- 426 Shebanits, O., Wahlund, J.-E., Edberg, N.J.T., Crary, F. J., Wellbrock, A., Andrews, D.
427 J., Vigren, E., Desai, R. T., Coates, A. J., Mandt, K. E., Waite, J. H. (2016). Ion and
428 aerosol precursor densities in Titan's ionosphere: A multi-instrument case study. *Jour-
429 nal of Geophysical Research: Space Physics*, 121. <https://doi.org/10.1002/2016JA022980>.
- 430 Sulaiman, A. H., Kurth, W. S., Persoon, A. M., Meniotti, J. D., Farrell, W. M., Ye, S.-Y.,
431 Hadid, L. Z. (2017). Intense harmonic emissions observed in Saturn's ionosphere. *Geo-
432 physical Research Letters*, 44, 12,049-12,056. <https://doi.org/10.1002/2017GL076184>.

- 433 Sulaiman, A. H., Kurth, W. S., Hospodarsky, G. B., Averkamp, T. F., Persoon, A. M., Me-
434 nietti, J. D., Ye, S.-Y., Gurnett, D. A., Farrell, W. M., Dougherty, M. K. (2018). Auroral
435 hiss emissions during Cassini's Grand Finale: Diverse electrodynamic interactions
436 between Saturn and its rings. *Geophysical Research Letters*, this issue.
- 437 Vigren, E., Galand, M., Yelle, R.V., Cui, J., Wahlund, J.-E., Ågren, K., Lav-
438 vas, P.P., Mueller-Wodarg, I.C.F. et al. (2013). On the thermal electron
439 balance in Titan's sunlit upper atmosphere. *Icarus*, 223, 1, 234-251.
440 <https://doi.org/10.1016/j.icarus.2012.12.010>.
- 441 Vigren, E., Galand, M., Shebanits, O., Wahlund, J.-E., Geppert, W. D., Lavvas, P., Vuit-
442 ton, V., Yelle, R. V. (2014). Increasing Positive Ion Number Densities below the Peak of
443 Ion-Electron Pair Production in Titan's Ionosphere. *The Astrophysical Journal*, 786(1),
444 69. <https://doi.org/10.1088/0004-637X/786/1/6>.
- 445 Wahlund, J.-E., André, M., Eriksson, A.I.E., Lundberg, M., Morooka, M. W., Shafiq, M.,
446 Averkamp, T.F., Gurnett, D. A., Hospodarsky, G. B., Kurth, W. S., Jacobsen, K. S.,
447 Pedersen, A., Farrell, W., Ratynskaia S. and Piskunov, N. (2009). Detection of dusty
448 plasma near the E-ring of Saturn. *Planetary and Space Science*, 14, 57, 1795–1806.
449 <https://doi.org/10.1016/j.pss.2009.03.011>.
- 450 Wahlund, J.-E., Morooka, W. M., Hadid, L. Z., Persoon, A. M., Farrell, W. M., Gurnett, D.
451 A., Hospodarsky, G., Kurth, W. S., Ye, S.-Y., Andrews, D. J., Edberg, N. J. T., Eriksson
452 A. I., and Vigren E. (2017). In Situ Measurements of Saturn's Ionosphere show it is
453 Dynamic and Interacts with the Rings. *Science*. <https://doi.org/10.1126/science.aao4134>.
- 454 Wahlund, J.-E., Vigren, E., Morooka, W. M., Hadid, L. Z., Farrell, W. M., Kurth, W. S.,
455 Moore, L., Galand, M., Nagy, A. F., Mitchel, D. G., Cravens, T. E., Waite, T. E. Jr.,
456 (2018). On the Characteristics of Charged Dust in Saturn's Equatorial Ionosphere-
457 implications from Cassini RPWS/LP data *Geophysical Research Letters*, this issue.
- 458 Waite, J.H., Jr., R. Perryman, M. Perry, K. Miller, J. Bell, T.E. Cravens, C.R. Glein, J.
459 Grimes, M. Hedman, T. Brockwell, B. Teolis, L. Moore, D. Mitchell, A. Persoon, W.S.
460 Kurth, J.-E. Wahlund, M. Morooka, L. Z. Hadid, S. Chocron, J. Walker, A. Nagy, R.
461 Yelle, S. Ledvina, R. Johnson, W. Tseng, O.J. Tucker and W.-H. Ip (2018), submitted to
462 Science.

Figure 1.

Author Manuscript

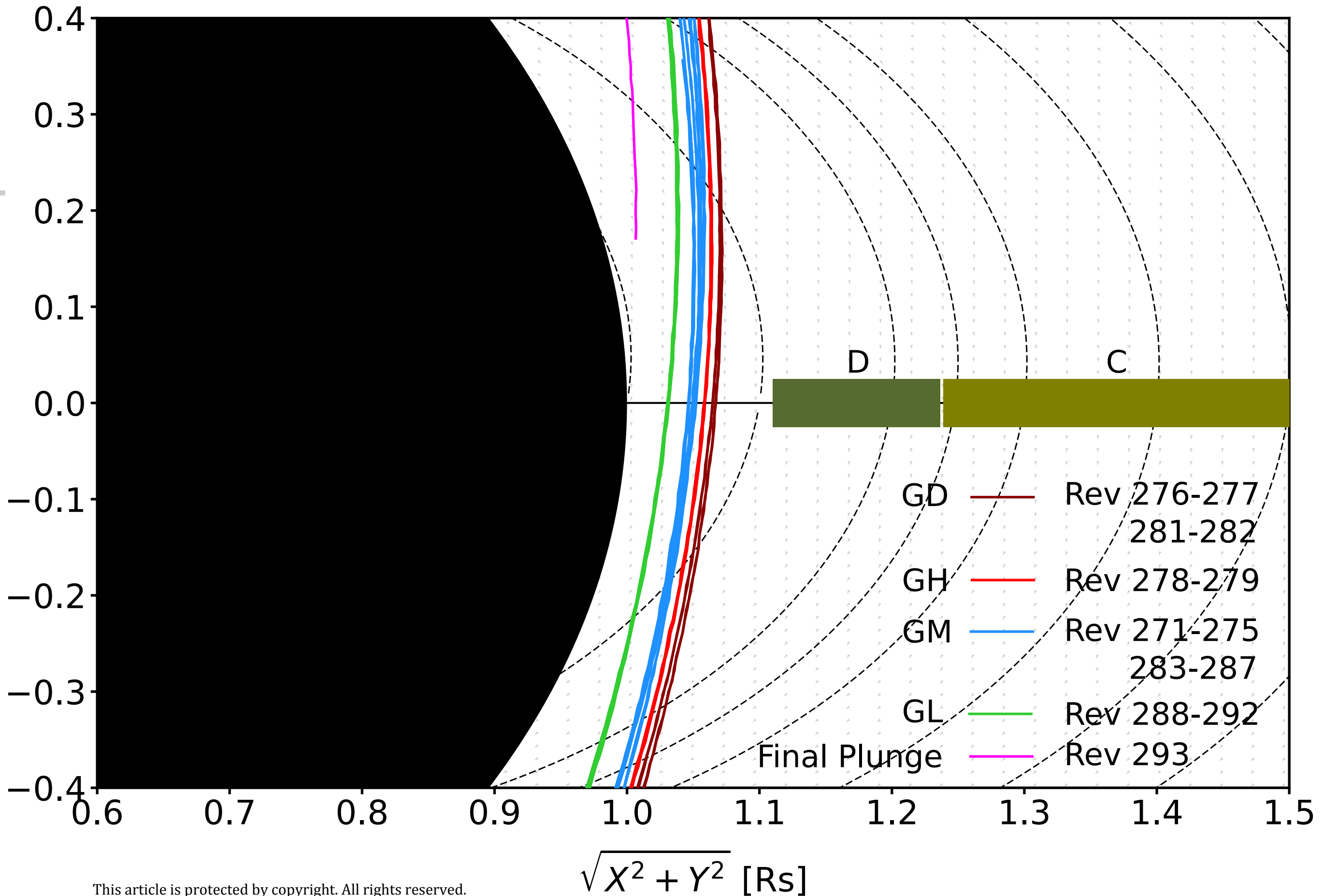


Figure 2.

Author Manuscript

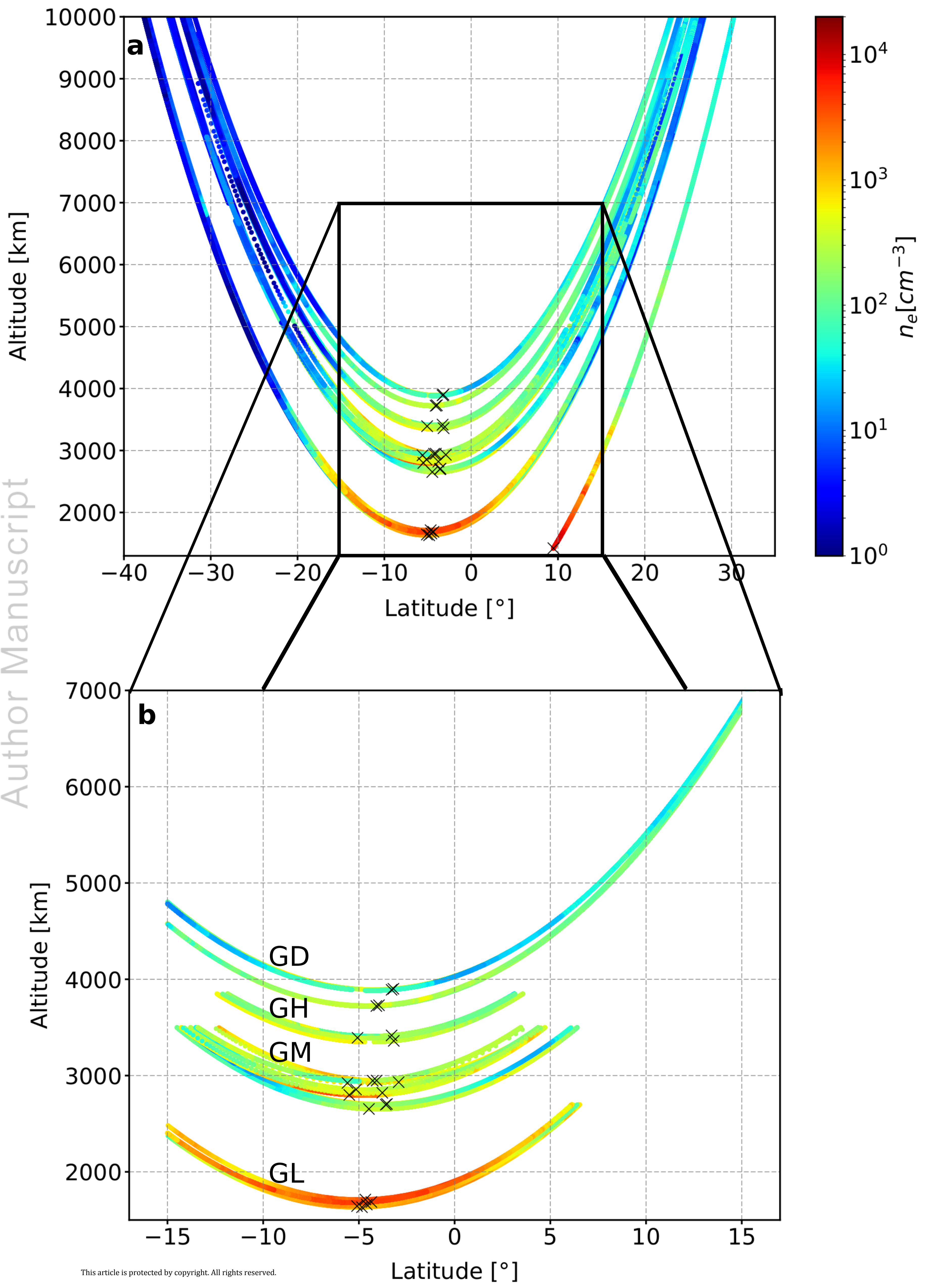
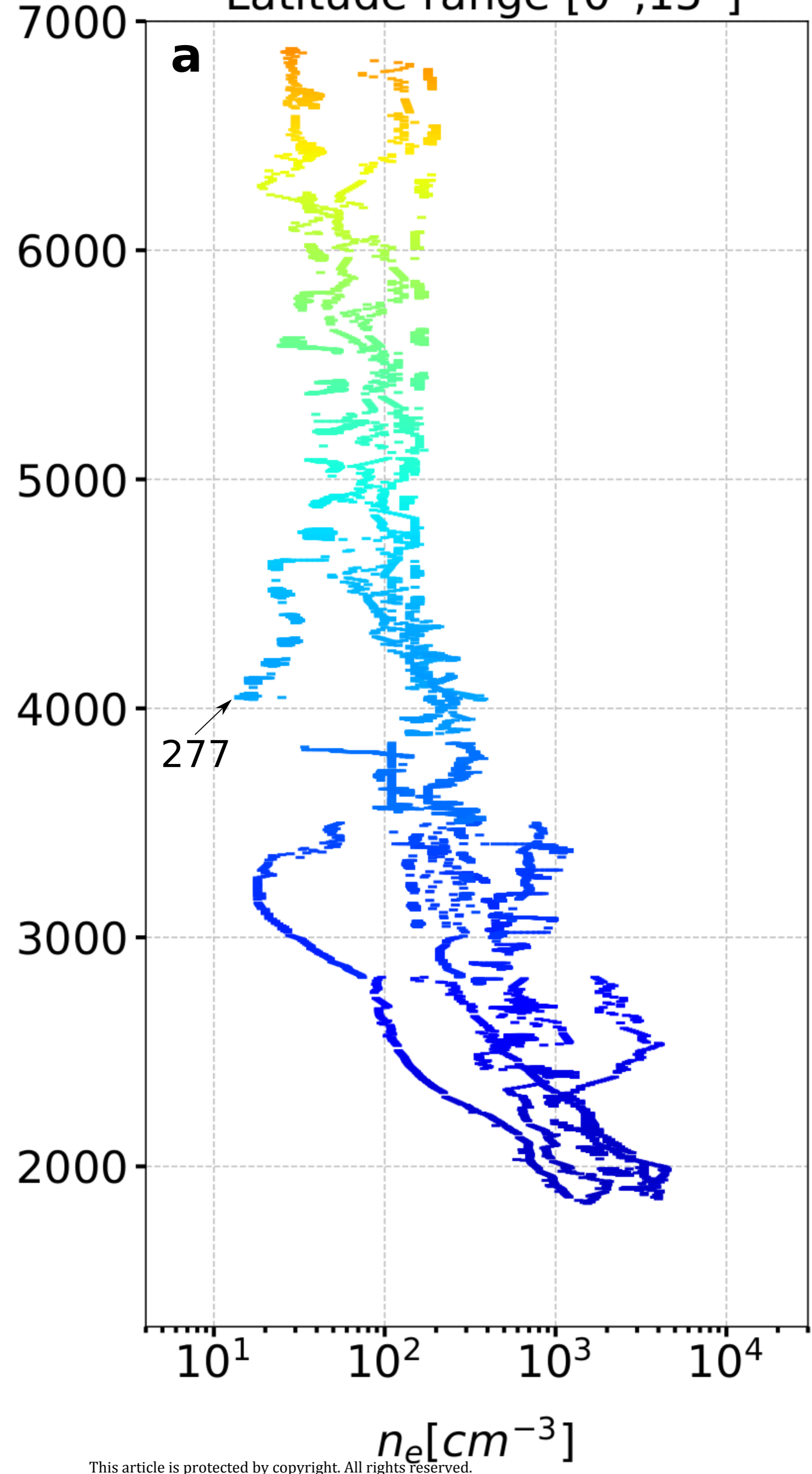


Figure 3.

Author Manuscript

Northern hemisphere
Latitude range [0°,15°]



Southern hemisphere
Latitude range [-15°,0°]

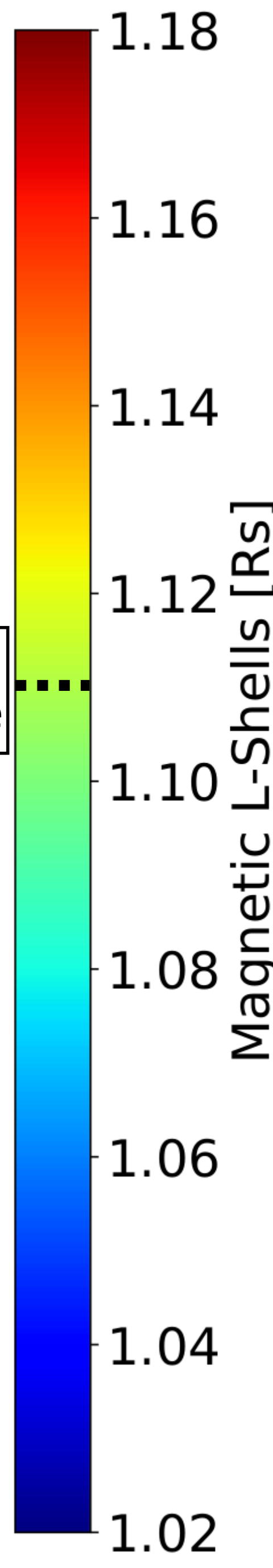
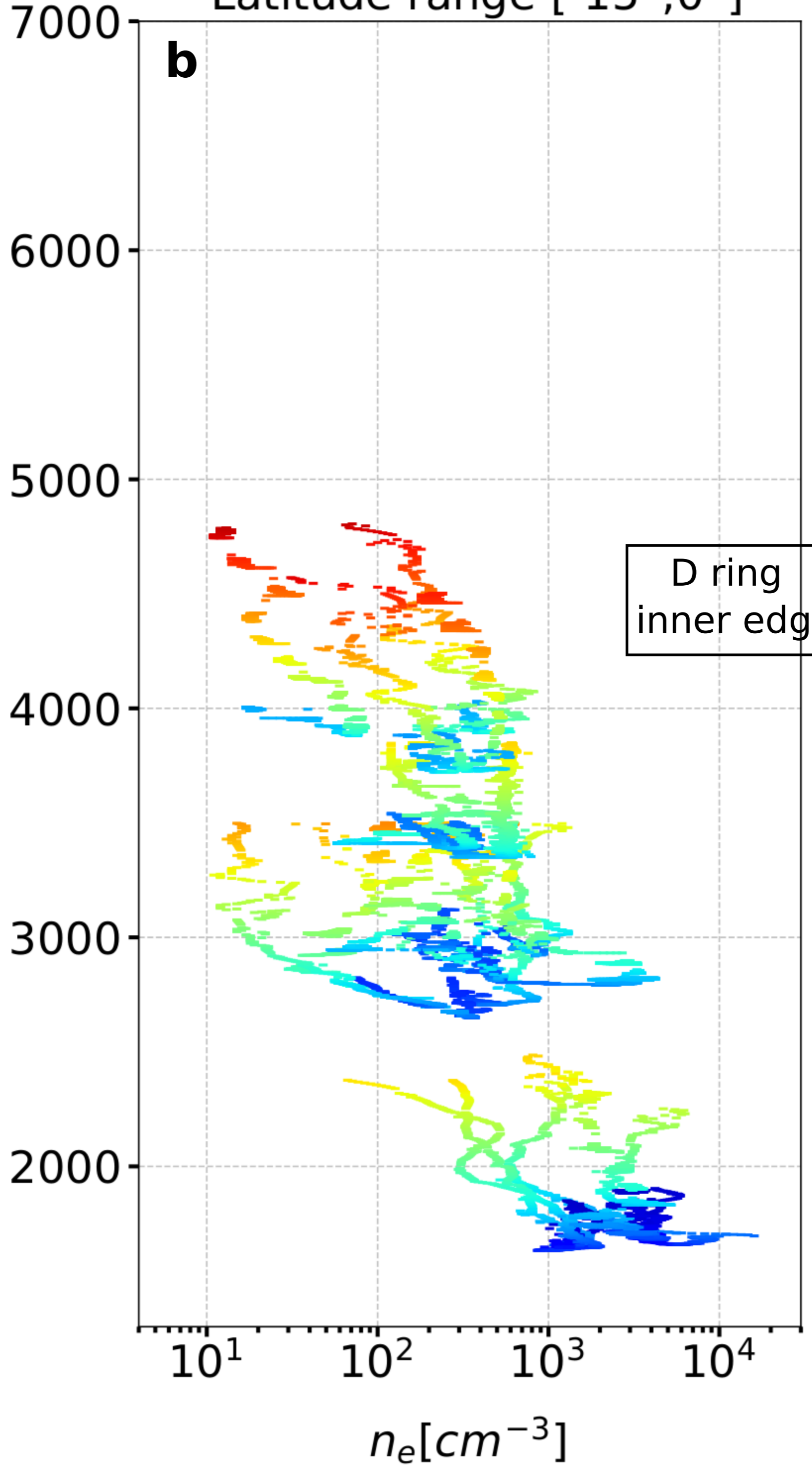
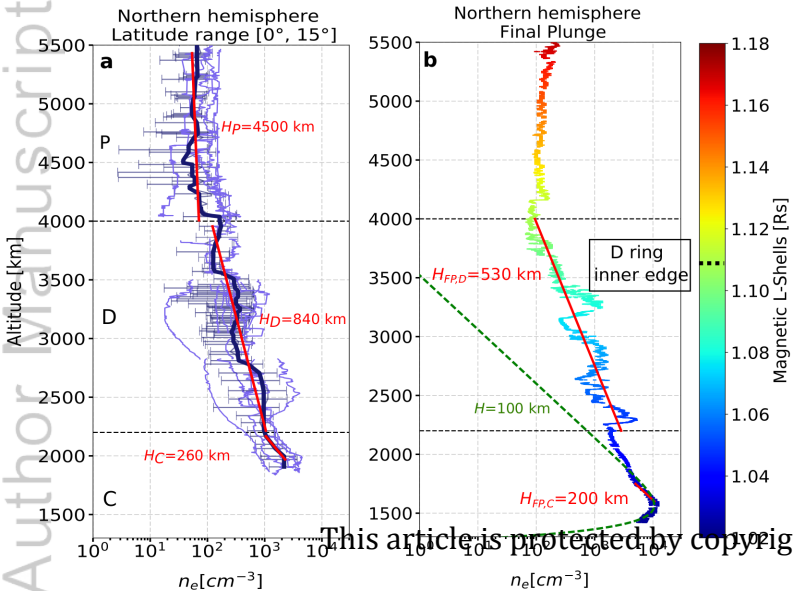
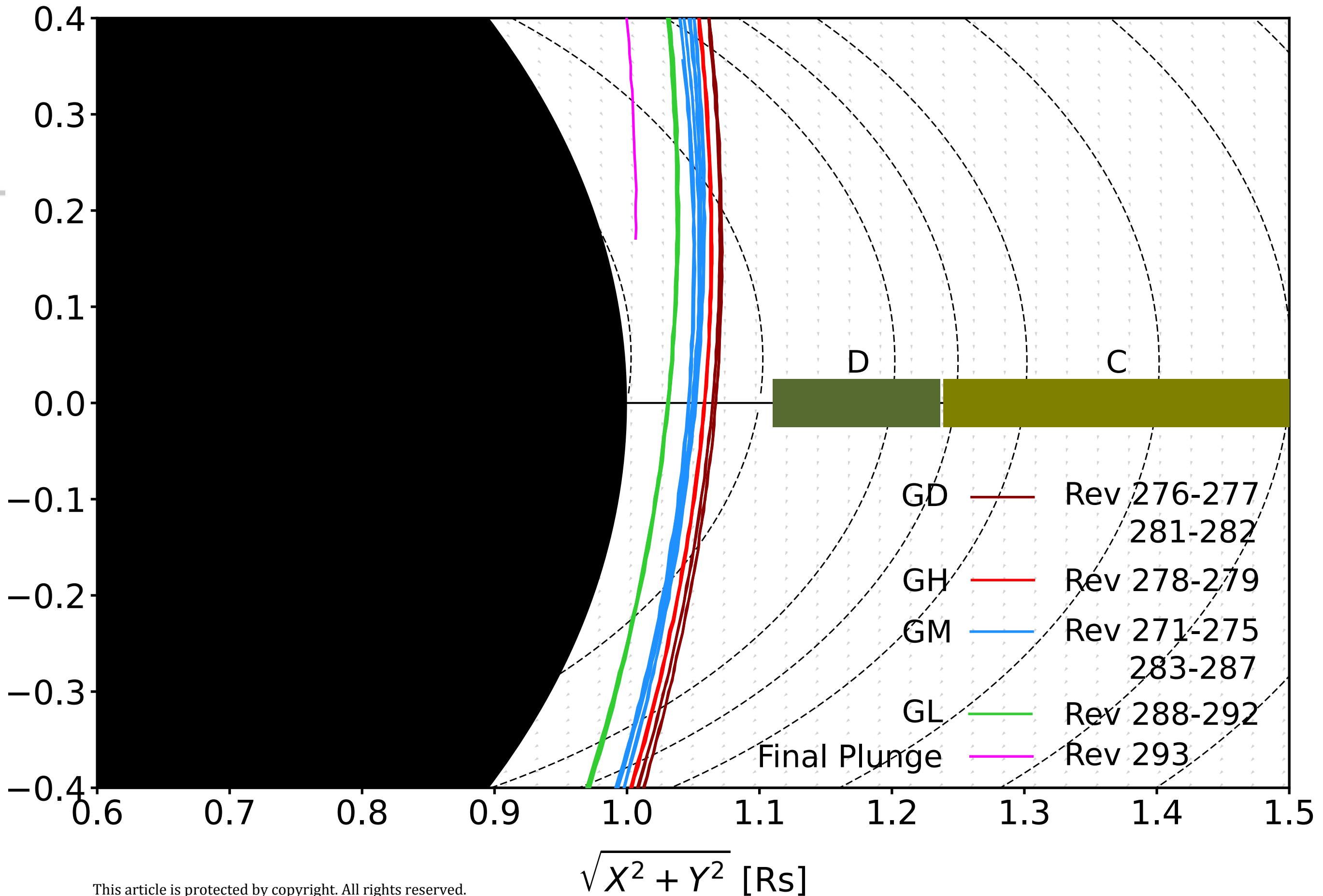
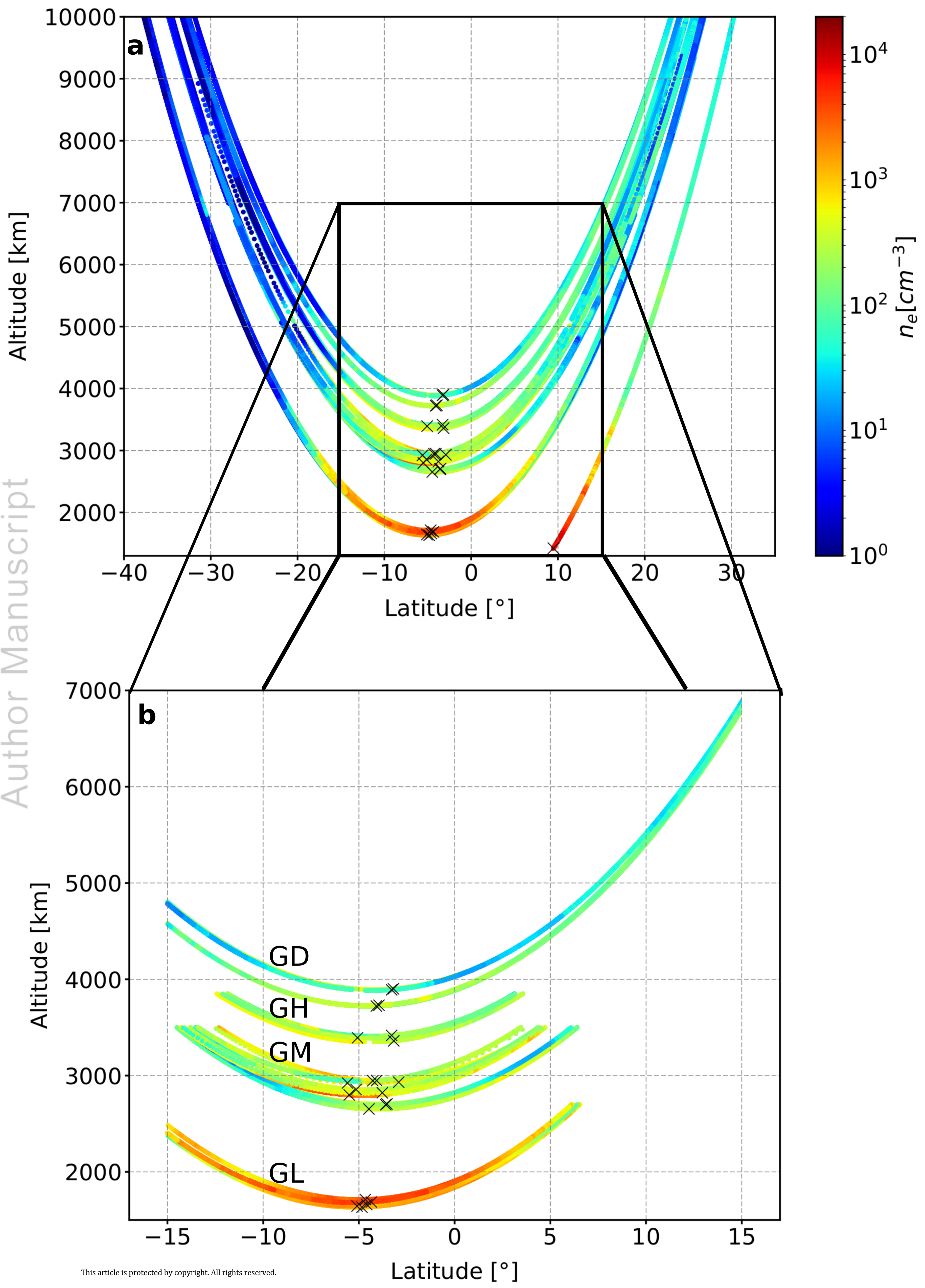


Figure 4.

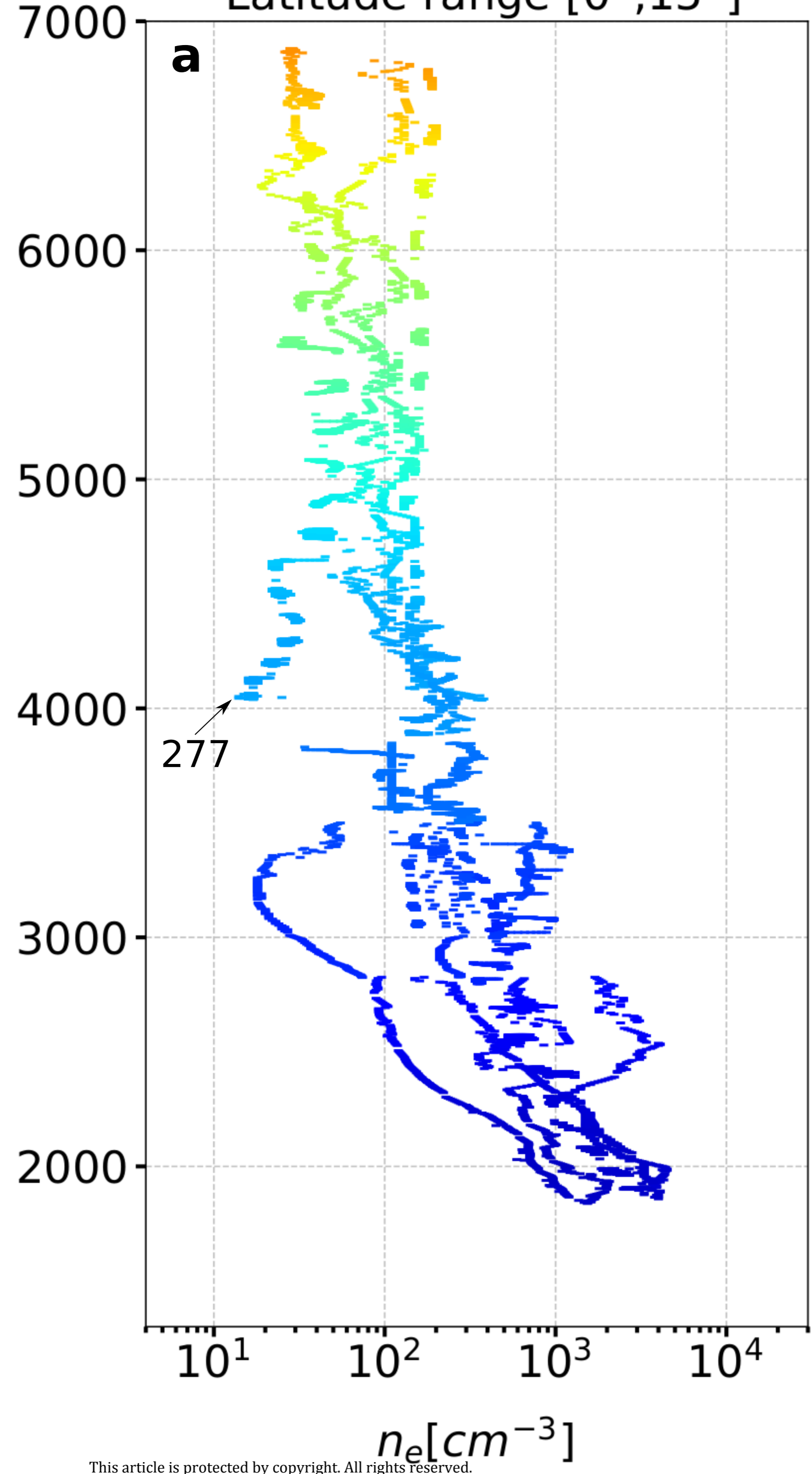
Author Manuscript







Northern hemisphere
Latitude range [0°,15°]



Southern hemisphere
Latitude range [-15°,0°]

